Journal of Materials Chemistry A

ROYAL SOCIETY OF CHEMISTRY

PAPER

View Article Online
View Journal | View Issue

Cite this: J. Mater. Chem. A, 2024, 12, 16735

Achieving high overall energy storage performance of KNN-based transparent ceramics by ingenious multiscale designing†

Zixiong Sun, ‡*abcde Shibo Zhao,‡[a] Ting Wang,‡[c] Hongmei Jing,*[f] Qing Guo,[a] Ruyue Gao,[a] Liming Diwu,[a] Kang Du,[g] Yongming Hu *[b] and Yongping Pu*[e]

Dielectric capacitors show significant advantages of faster charge–discharge time over solid oxide fuel cells, Li-ion batteries, and electrochemical capacitors and have been considered the best candidates for next-generation high-performance pulsed power systems. Considering the advantage of the feasibility of efficient multifunctional coupling, which meets the integration trend of electronic devices and relies on the excellent transmittance of KNN-based ceramics, we chose KNN-based systems in this work. $(1-x)(K_{0.5}Na_{0.5})NbO_3$–$xBa_{0.9}Ca_{0.1}Zr_{0.15}Ti_{0.85}O_3$ ceramics were fabricated by employing conventional solid state technology, and as expected, the substitution of Ba/Ca by K/Na in the A-site and the substitution of Zr/Ti by Nb in the B-site strongly decreased the leakage current of pristine KNN. By multiscale designing, a W_{rec} of 7.83 J cm^{-3} with an η of 81.02%, which has huge advantages over both BCZT-based systems and KNN-based systems, was finally achieved when the x equals 0.30, and such an excellent energy storage performance was caused by both high maximum polarization and high large electric breakdown strength. According to their microstructure characterization, the former was caused by the existence of high polarization boundaries induced by the lattice mismatch between the two phases, and the latter was proved by the combined effect of conductive mechanism transition and interface engineering. In addition, relatively high energy storage frequency stability, thermal stability, and polarization fatigue endurance were also obtained, and the charge–discharge behavior indicated their potential in practical applications. The work offered a new concept for designing energy storage capacitors with high overall performance.

Received 8th April 2024
Accepted 27th May 2024

DOI: 10.1039/d4ta02425g

rsc.li/materials-a

1 Introduction

Despite their faster charge–discharge speed over the other three most commonly used battery systems, which are Li-ion batteries, fuel cells, and super-capacitors, energy storage capacitors have been suffering from the drawback of short battery life for quite a long time,[1–6] and their development was thus limited. Such a problem is mainly due to the paradox of obtaining large polarization and high electric breakdown strength simultaneously, which have already been reported in many previous studies. Taking the common strategy of domain engineering as an example, based on the physical description in eqn (S1),† refining the domain size for increasing the electric breakdown strength (E_b) indeed works in improving the energy storage density (W_{rec}) to some extent; the polarization degradation, which happens at the same time, however, shows a negative effect.[7–10] A similar issue also exists in studies of film state materials, which always focus on interface engineering. In those cases, artificially introduced interfacial dipole moments strongly improve the total maximum polarization (P_{max}) under a high electric field. Nevertheless, the charge accumulation near the interfaces also weakens the voltage endurance for the inevitable increase in ionic conductance.[11–14] It is worth noting that compared to film state materials, including both epitaxial thin films and ceramic-polymer hybrid films, bulks store more energy and show more significant potential in applying to large-scale pulsed power equipment; we will thus try to solve the

[a]School of Electronic Information and Artificial Intelligence, Shaanxi University of Science and Technology, Xi'an 710021, PR China. E-mail: SunZX@sust.edu.cn

[b]Hubei Key Laboratory of Micro-Nanoelectronic Materials and Devices, Hubei University, Wuhan 430062, China. E-mail: huym@hubu.edu.cn

[c]Guangdong Provincial Key Laboratory of Electronic Functional Materials and Devices, Huizhou University, Huizhou 516001, Guangdong, China

[d]School of Materials Science and Engineering, Shaanxi University of Science and Technology, Xi'an 710021, PR China

[e]MESA+ Institute for Nanotechnology, University of Twente, PO Box 217, 7522 NH Enschede, The Netherlands. E-mail: puyongping@sust.edu.cn

[f]School of Physics and Information Technology, Shaanxi Normal University, Xi'an, 710119, PR China. E-mail: jhmei.dengdai@snnu.edu.cn

[g]School of Mathematical and Physical Sciences, Wuhan Textile University, Wuhan, 430200, China

† Electronic supplementary information (ESI) available. See DOI: https://doi.org/10.1039/d4ta02425g

‡ Z. Sun, S. Zhao, and T. Wang contributed equally to this work.

abovementioned paradox to enhance the energy storage capacity of bulk state materials in this work.

Based on the research of the last two decades, the bulk systems for energy storage have been summarized to be bismuth sodium titanate (BNT)-based, strontium titanate (STO)-based, barium titanate–$BiMeO_3$ (BT–$BiMeO_3$)-based, silver niobate (AN)-based, and potassium-sodium niobate (KNN)-based systems.[6] Due to the feasibility of efficient multi-functional coupling, which relies on their excellent transmittance and shows huge potential when applied in the military, KNN-based systems have attracted continuous attention from researchers for quite a long time.[15,16] KNN-based ceramics' transmittance can also be easily modified by controlling the grain size, crystal structure, density (pores), and domain walls.

But because of the large grain size and volatility of K and Na, pristine KNN suffers from inferior transparency and high leakage current, respectively, and according to what has been reported in the literature, inhibiting the grain growth by obstructing the mass transfer during the sintering process[17,18] and heterovalent substitution[19] have successfully figured these problems out. Though these two kinds of technologies are pretty mature now, the paradox mentioned above has yet to be solved entirely,[20] and the energy storage capacity of KNN-based ceramics still needs to be improved. Modulation within a single degree of freedom seems impossible to satisfy our desire, so the effective solution should lie in a synergistic effect. The $Ba_{1-x}Ca_xZr_yTi_{1-y}O_3$ (BCZT) system is a complex solid solution of $BaTiO_3$ (BT), in which the Ca and Zr atoms occupy the A-site and B-site, respectively. It not only has the adjustability of dielectric and ferroelectric properties but also shows the simplicity of obtaining multi-phase structures. The W_{rec} enhancement in BCZT-based relaxor ferroelectrics has also been successfully achieved *via* interface-assisted large polarization in our previous work.[21] Motivated by this, in this work, we incorporated BCZT into the KNN lattice to form $(1-x)(K_{0.5}Na_{0.5})NbO_3$–$xBa_{0.9}Ca_{0.1}Zr_{0.15}Ti_{0.85}O_3$ ($(1-x)$KNN–xBCZT) solid solutions. Through multiscale designing: (1) the leakage current was decreased due to the inhibition of electron production; (2) the high polarization boundaries (HPBs), which were induced by the lattice mismatch between the two different phases, were thought to be the reason for the interfacial polarization; (3) the combined effect of the conducting mechanism transition and the interface's blocking effect led to high E_b. Finally, excellent energy storage performances with high energy storage reliability were reached in such transparent ceramics.

2 Experimental section

Details of this part are provided in the ESI.†

3 Results and discussion

3.1 Characterization of the phase and structure

Fig. 1(a) shows the photo of the $(1-x)$KNN–xBCZT ceramics with x from 0.10 to 0.50. All of them are transparent, and the one with $x = 0.3$ has the best transparency (the reason for this will be discussed later). The optical transmittance was also measured and is displayed in Fig. S1(a).† Fig. 1(b1) shows the scanning electron microscope (SEM) image of 0.7KNN–0.3BCZT, and those of $(1-x)$KNN–xBCZT with $x = 0.1$, 0.3, and 0.5 are displayed in Fig. S1(b1)–(b3),† with the grain size distribution in the inset. The average grain size decreases from 1.47 μm to 0.70 μm and then to 0.54 μm, indicating the effect of grain size refinement after the BCZT doping. Fig. 1(b2)–(b5) show the energy disperse spectroscopy (EDS) mappings for K, Ti, Nb, and Ba of the area circled by the red dashed rectangle of Fig. 1(b1), and all of these elements are pretty evenly distributed. Fig. S2† displays the result of the Rietveld XRD refinement of all the $(1-x)$KNN–xBCZT ceramics with the corresponding ball–stick models displayed in each figure. The lattice parameters are summarized in Table S1.† The variation between the lattice parameter and the BCZT doping content is plotted in Fig. 1(c1) and (c2). Pure KNN ceramic possesses the orthorhombic phase (O-phase) with the space group of *Bmm*2, which agrees with a previous report,[22] and the ceramic is transferred to the tetragonal phase (T-phase) with the space group of *P*4*mm* when the x is 0.1. The two-phase co-existence of the T-phase and O-phase with the space group of *P*222 was obtained when the x reaches 0.3, and the single structure of *P*222 is observed in all the remaining components. The R_{wp}, R_p, and χ^2 values, which describe the weighted profile parameter, the unweighted profile parameter, and the goodness of fit of each sample, respectively, are also added in Table S1.† According to their values, such a refinement is highly credible. For more microstructure information, we performed a transmission electron microscopy (TEM) test on $(1-x)$KNN–xBCZT ceramics with $x = 0.1$, 0.3, and 0.5, and the images are displayed in Fig. 1(d1)–(d3). Stripe-like 180° domains were seen in the 0.9KNN–0.1BCZT, as shown in Fig. 1(d1), indicating a large polarization retention.[23] Domains with a much smaller size, circled by the red dashed line in Fig. 1(d2), can be observed when the BCZT doping content is increased to 0.3, indicating the transformation from a typical ferroelectric (FE) to a relaxor ferroelectric (RFE).[8,24,25] When the BZT doping content is further increased to 0.5, almost no domains can be detected, as seen in Fig. 1(d3), in which case the behavior of a linear dielectric can be predicted. After the microstructure observation, first-order reversal curve (FORC) measurements were also carried out to theoretically analyze the structure–function relationship. By gradually increasing the reversal electric field (β) with a fixed applied electric field (α) of 180 kV cm^{-1}, the diagrams for the FORC distribution were drawn and are displayed in Fig. 1(e1)–(e3). The corresponding waveforms of the ferroelectric hysteresis (P–E) loops are provided in Fig. S3,† and the details of FORC measurements are presented in the Experimental section. As expected, the diagram with the highest-intensity distribution zone in the central region, which results from the large polarization retention, is found in 0.9KNN–0.1BCZT, as mentioned above. For the diagram of 0.7KNN–0.3BCZT, quite a lower polarization retention than the former can be predicted based on its tiny but non-zero, low-intensity distribution zone. The ceramic with a further BZT doping content of 0.5 indicates more even FORC distribution and thus stronger linear dielectric behavior. For more in-

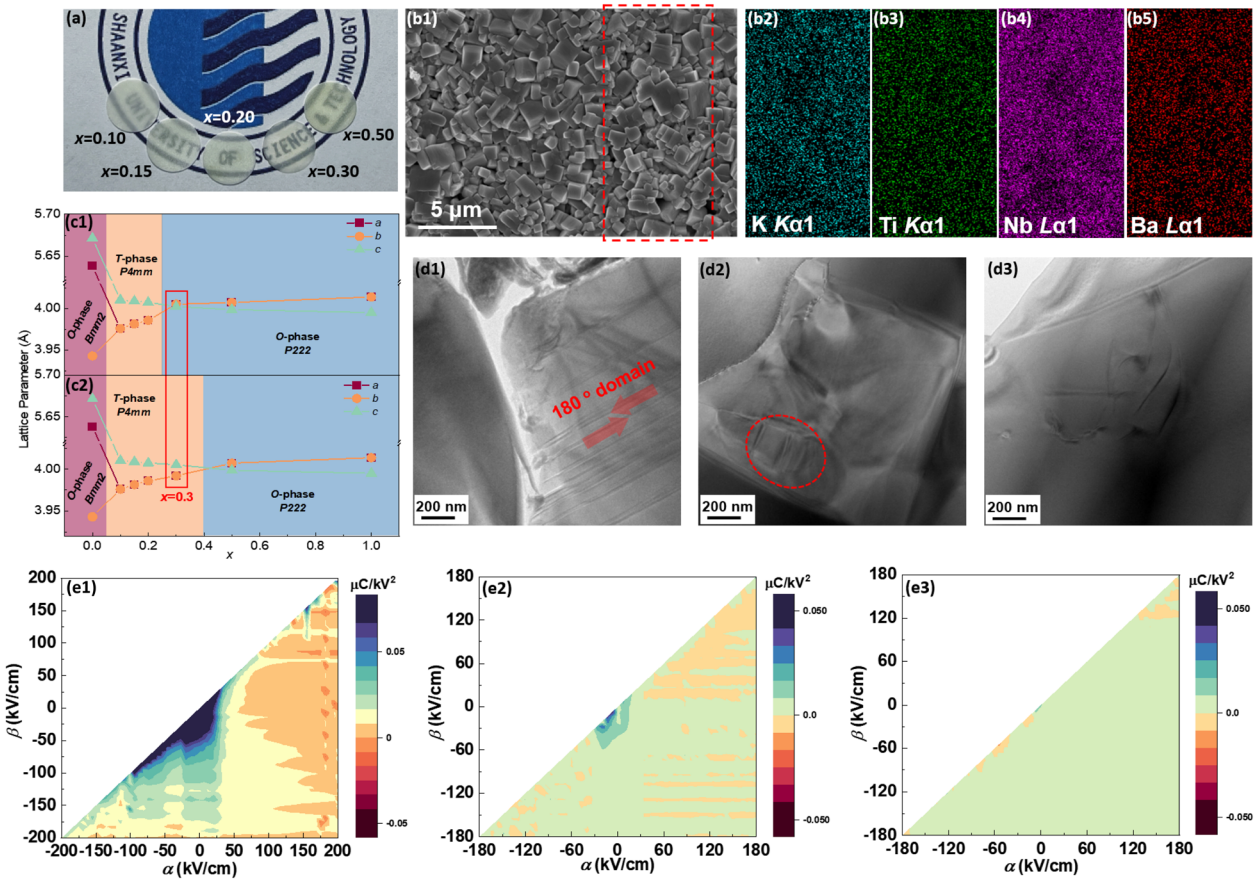

Fig. 1 (a) Picture of $(1-x)$KNN–xBCZT ceramics with different x; (b1) SEM image of 0.7KNN–0.3BCZT; (b2)–(b5) EDS mappings for K, Ti, Nb, and Ba of the area circled by the red dashed rectangle in (b1); (c1) and (c2) the variation between the lattice parameter and x; (d1)–(d3) TEM images of $(1-x)$KNN–xBCZT ceramics with $x = 0.1$, 0.3, and 0.5; (e1)–(e3) the FORC distribution of $(1-x)$KNN–xBCZT ceramics with $x = 0.1$, 0.3, and 0.5.

depth characterization, the HAADF-STEM images of $(1-x)$KNN–xBCZT ceramics with $x = 0.1$, 0.3, and 0.5 along the [100] crystal axis were recorded. According to the displacement of B-site atoms (weaker contrast) relative to the center of the four adjacent A-site atoms (stronger contrast), the orientation of spontaneous polarization (P_s) of ceramics can be thus confirmed.[26,27] 0.9KNN–0.1BCZT and 0.5KNN–0.5BCZT show the single T-phase and O-phase with upward and rightward P_s orientation, respectively, as detected in Fig. 2(a1) and (a3). This is consistent with the results of the Rietveld XRD refinement. Similarly, the coexistence of the T-phase and O-phase of 0.7KNN–0.3BCZT can also be confirmed in Fig. 2(a2), and the orange dashed line is the boundary between these two phases, in which the polarization transition region can be seen. Fig. 2(b1)–(b3) show the fast Fourier transform (FFT) images that transformed from Fig. 2(a1)–(a3) using Gwyddion, and the separated patterns indicate the single crystal characteristic of the selected areas for all the ceramics. When zooming in the $(30\bar{3})$ plane of Fig. 2(b2), as shown in Fig. 2(b4), two different patterns, which correspond to the T-phase and O-phase, can be seen, again proving the two-phase coexistence in 0.7KNN–0.3BCZT.

3.2 Results of the energy storage performance

Before knowing the energy storage performance of the $(1-x)$KNN–xBCZT ceramics, the E_b, which is generally obtained *via* the Weibull distribution of each sample, needs to be calculated, and the details for such a statistical calculation are provided in the ESI.† The result of the Weibull distribution is shown in Fig. 3(a) after measuring 12 different electrodes (each one was considered as one capacitor) in the ceramic of the same component, and the E_b of each ceramic is given in the insert. Finally, the best voltage endurance with an E_b of 604.07 kV cm^{-1} is found in the $(1-x)$KNN–xBCZT ceramic with $x = 0.3$. The unipolar P–E loops of all these ceramics from 20 kV cm^{-1} to their E_b are shown in Fig. S4,† and the corresponding W_{rec} and energy storage efficiency (η) were calculated, and the variation between them and the applied electric field is plotted in Fig. 3(b). To make a comparison within these ceramics, the P–E loops at the E_b of all the ceramics are summarized at the bottom of Fig. 3(c), and on the top, the variation between both W_{rec} and η and x is also plotted. The highest W_{rec} of 7.83 J cm^{-3} with an η of 81.02% was achieved in 0.7KNN–0.3BCZT. To show the advantage of the energy storage performance of our $(1-x)$KNN–xBCZT ceramics among the up-to-date BCZT- and KNN-based systems, a comparison diagram, in which the X-axis and Y-axis

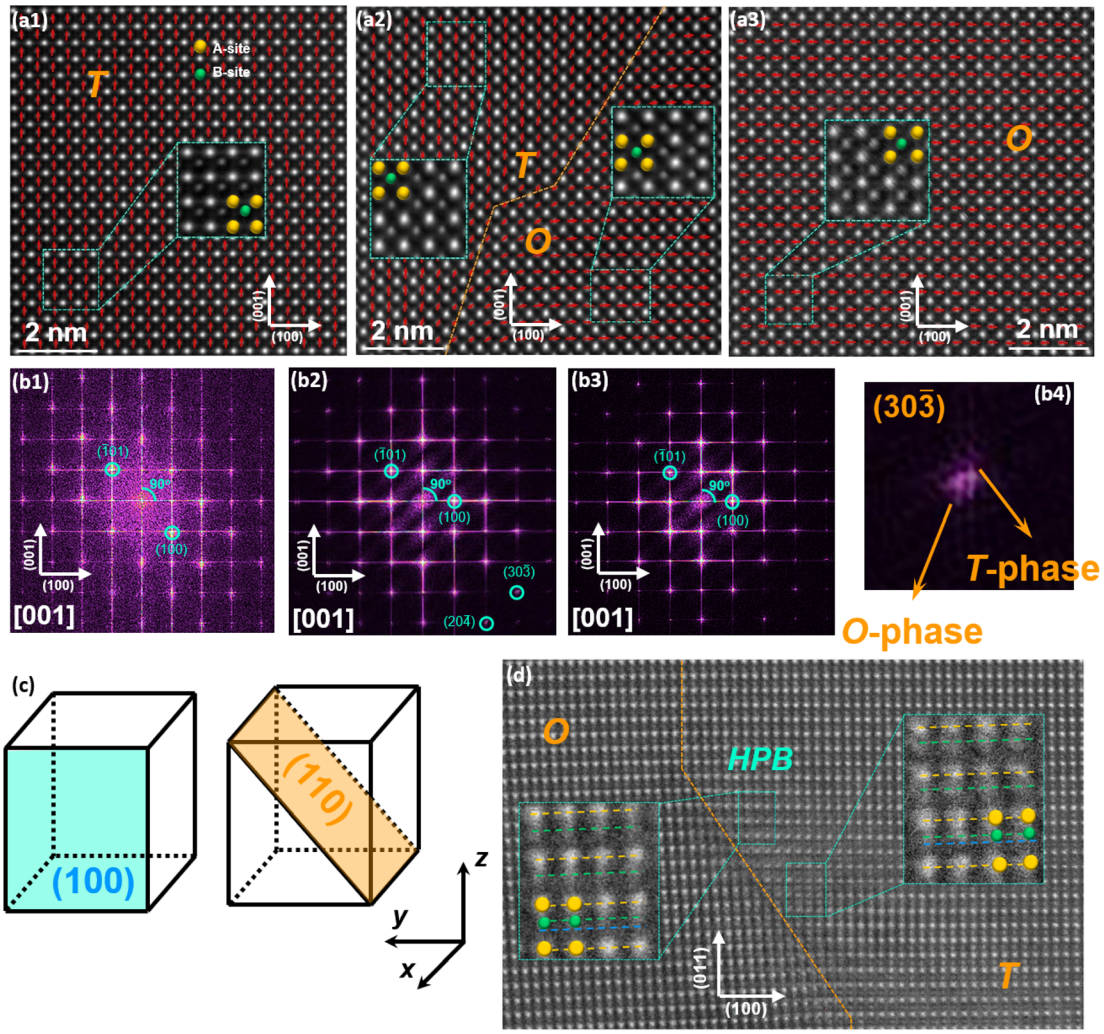

Fig. 2 (a1)–(a3) The HAADF-STEM images of $(1-x)$KNN–xBCZT ceramics with $x = 0.1$, 0.3, and 0.5 along the [100] crystal axis, and the illustrations in the pictures are the enlarged views of the areas circled by green rectangles; (b1)–(b3) the fast Fourier transform (FFT) images that transformed from (a1)–(a3) using Gwyddion; (b4) enlarged view around the (30) plane of (b2); (c) sketch to show the (100) and (110) planes in the perovskite structure; (d) HAADF-STEM images of the 0.7KNN–0.3BCZT ceramic along the [110] crystal axis, the dislocation can be found between different phases and the B-site atoms near the boundary have relatively large displacement.

are W_{rec} and η, respectively, is illustrated in Fig. 2(d).[16,28–56] It can be seen that our ceramics have apparent advantages in energy storage capacity among both systems.

3.3 Discussion of the polarization

Fig. 4(a) and (b) show the P–E loops of $(1-x)$KNN–xBCZT at 20 kV cm^{-1} (low field) and 180 (high field) kV cm^{-1}, respectively, and the variations between their P_{max} with the difference between them and BCZT doping content are plotted in Fig. 4(c). These results show that the $(1-x)$KNN–xBCZT ceramics with lower x show fatter loops and higher P_{max}, demonstrating their higher leakage current, and the loop becomes slimmer with increasing x. The higher leakage current can be explained as follows: the lattice-oxygen atoms changed to oxygen and escaped at high sintering temperature, leaving the oxygen vacancies and electrons in the ceramic lattices, as expressed in eqn (1)

$$O_O \rightarrow \frac{1}{2}O_2 + V_{\ddot{O}} + 2e' \quad (1)$$

Because of the volatilization of K and Na in KNN, the following processes happened at the same time.

$$Na_{Na} + e' \rightarrow Na + V'_{Na} \quad (2)$$

$$K_K + e' \rightarrow K + V'_K \quad (3)$$

These two processes consumed electrons and facilitated the reaction of eqn (1);[19,57] more electrons were thus produced, resulting in the fat loops and higher P_{max} in $(1-x)$KNN–xBCZT ceramics with lower x. When BCZT was incorporated into the KNN lattice, Ba/Ca atoms occupied the K/Na sites, and the Nb sites were occupied by Ti/Zr atoms, as sketched in Fig. 4(f1) and

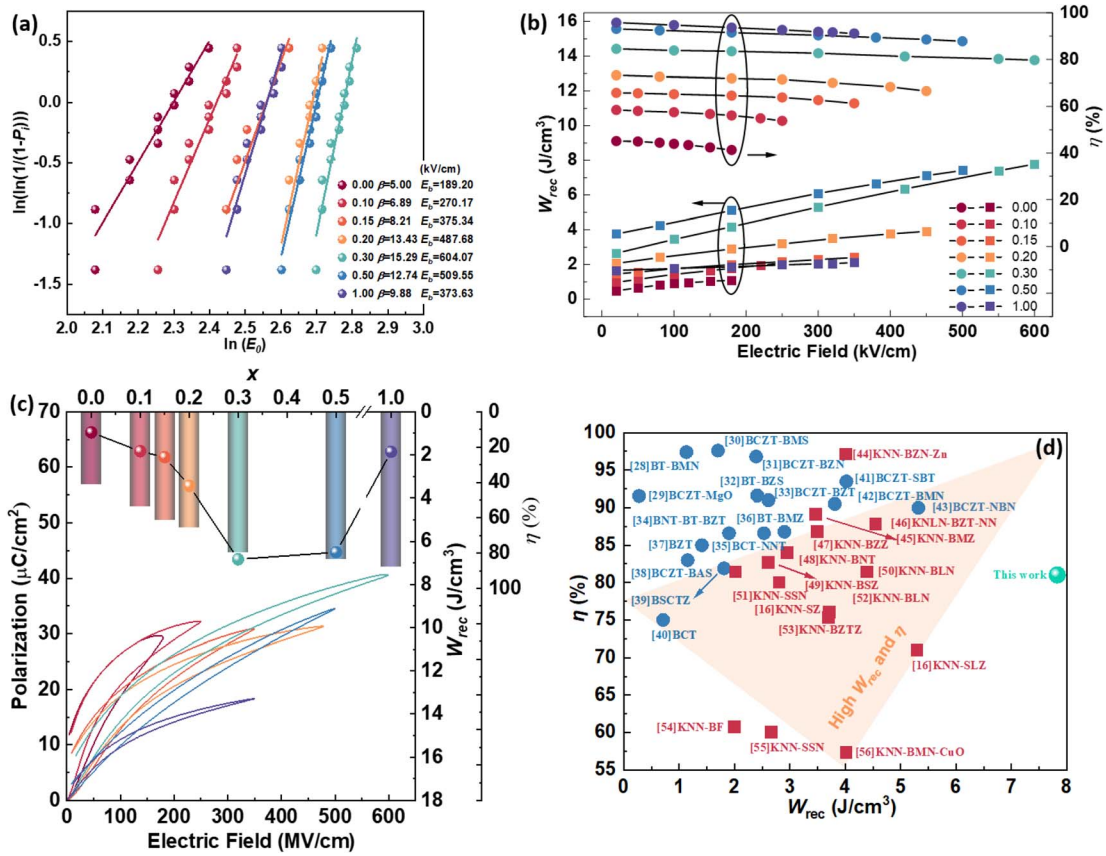

Fig. 3 (a) Weibull distribution of $(1-x)$KNN–xBCZT ceramics and the E_b of each one is shown in the inset; (b) the variation between both W_{rec} and η and applied electric field; (c) the P–E loops at E_b of all the ceramics are summarized at the bottom, and the W_{rec} and η of each ceramic are plotted on the top; (d) the comparison between the 0.7KNN–0.3BCZT ceramic in this work and some typical BCZT-based and KNN-based ceramics.[16,28–56]

(f2). The corresponding defect equations are expressed as follows:

$$BaO \xrightarrow{K_2O} Ba_K^{\cdot} + V_K^{'} + O_O \quad (4)$$

$$BaO \xrightarrow{Na_2O} Ba_{Na}^{\cdot} + V_{Na}^{'} + O_O \quad (5)$$

$$CaO \xrightarrow{K_2O} Ca_K^{\cdot} + V_K^{'} + O_O \quad (6)$$

$$CaO \xrightarrow{Na_2O} Ca_{Na}^{\cdot} + V_{Na}^{'} + O_O \quad (7)$$

$$2TiO_2 \xrightarrow{Nb_2O_3} 2Ti_{Nb}^{'} + V_O^{\cdot\cdot} + O_O \quad (8)$$

$$2ZrO_2 \xrightarrow{Nb_2O_3} 2Zr_{Nv}^{'} + V_O^{\cdot\cdot} + O_O \quad (9)$$

The newly formed $V_K^{'}$, $V_{Na}^{'}$, and $V_O^{\cdot\cdot}$ inhibited the reactions of eqn (1)–(3) so the number of free electrons was decreased. Here, we have to admit that though the amount of $V_O^{\cdot\cdot}$ with $Ti_{Nb}^{'}$ and $Zr_{Nb}^{'}$ also increases and the defect dipoles of $2Ti_{Nb}^{'} - V_O^{\cdot\cdot}$ and $2Zr_{Nb}^{'} - V_O^{\cdot\cdot}$ are thus formed, compared to the free electrons, such defect dipoles have much lower mobility so the leakage current will not increase but decrease. Also, the formation of these defect dipoles decreases the domain, leading to a slimmer P–E loop.[58,59] Due to this, the P_{max} decreases monotonously with increasing x at 20 kV cm^{-1}. Another proof for such defect equations comes from the electron paramagnetic resonance (EPR) measurement, as seen in Fig. 4(g). The g factor in the spectra is calculated according to eqn (10),

$$g = \frac{\hbar\nu}{\mu_B B} \quad (10)$$

in which $\hbar$, μ_B, ν, and B are the Planck constant, Bohr magneton, applied microwave frequency, and resonance magnetic field, respectively. A symmetrical peak around $g \sim 1.999$, which indicates the existence of $V_O^{\cdot\cdot}$, was observed in the $(1-x)$KNN–xBCZT ceramics with $x = 0.00$, 0.10, and 0.50.[60,61] Meanwhile the peak for proving the existence of Ti^{3+}, which is observed around $g \sim 1.982$, increases with increasing BCZT doping content. This is because substituting Nb^{3+} by Ti^{4+} resulted in extra Ti^{3+}, which agrees well with the above defect equations.[62] For the x dependence of P_{max} at 180 kV cm^{-1}, with increasing x, the P_{max} decreases first from 0 to 0.2, and then an abnormal enhancement can be seen at $x = 0.3$, and the P_{max} decreases again with further increase in doping content. As we have concluded from the results of XRD and TEM, the $(1-x)$

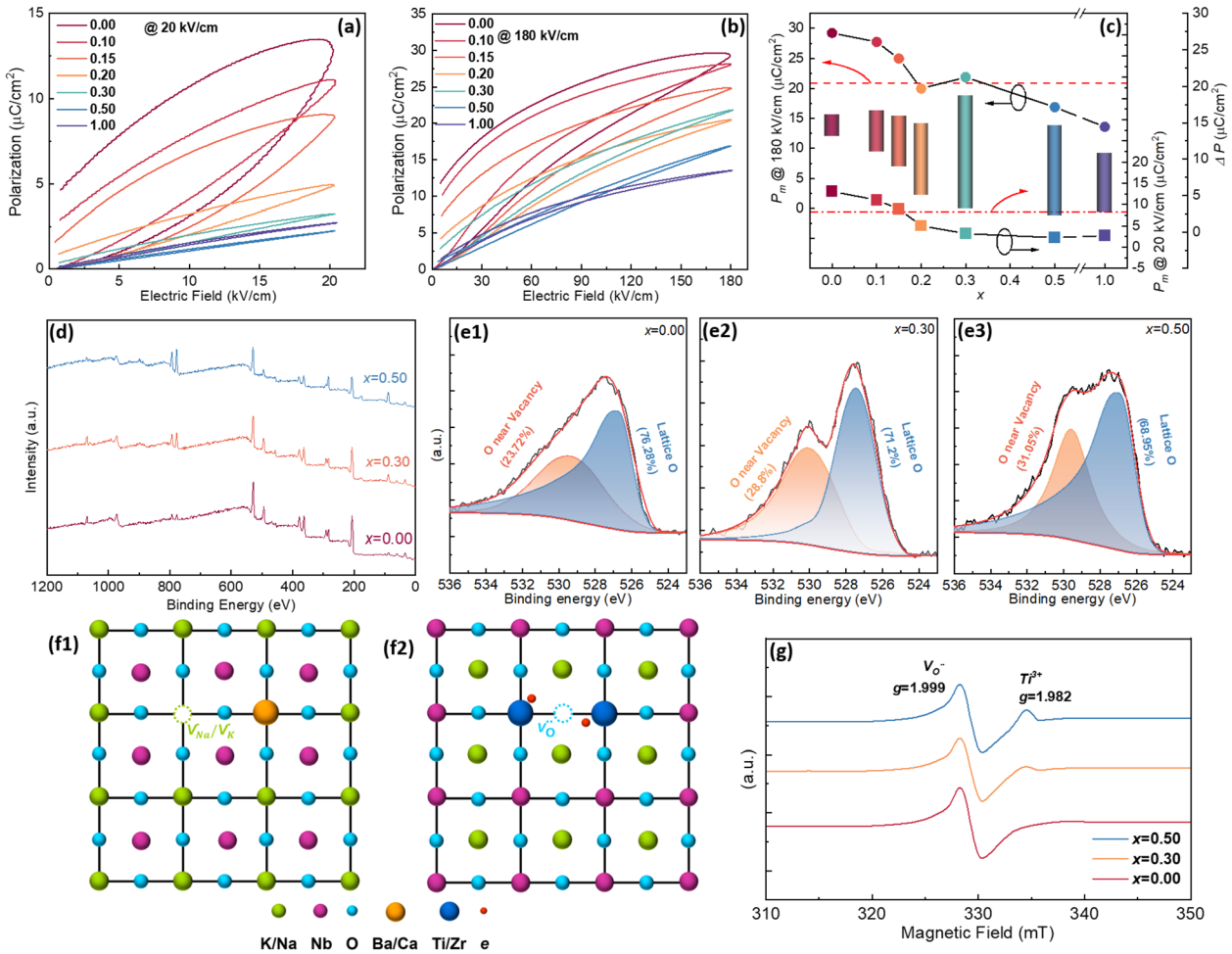

Fig. 4 The unipolar P–E loops of $(1-x)$KNN–xBCZT ceramics under (a) 20 kV cm^{-1}; (b) 180 kV cm^{-1}; (c) the variation between the P_m in (a) and (b) and x with the difference between them; (d) the XPS spectrum from 0–1200 eV; (e1)–(e3) the enlarged XPS spectrum from 524–536 eV; (g) the EPR spectrum of $(1-x)$KNN–xBCZT ceramics with $x = 0.00$, 0.30, and 0.50; (f1) and (f2) sketch of the A-O plane and B-O plane of the lattice of $(1-x)$KNN–xBCZT ceramics to explain eqn (1)–(9).

KNN–xBCZT ceramic with $x = 0.3$ shows the co-existence of the T-phase and O-phase, and the interfacial polarization might cause such an abnormal enhancement of polarization. To reveal this, we took the HAADF-STEM images of $(1-x)$KNN–xBCZT with $x = 0.3$ along the [110] crystal axis, as displayed in Fig. S5,† and the sketch to show the relative position of (001) and (110) planes is illustrated in Fig. 2(c). The orange line in Fig. S5† represents the phase boundary between the two different phases, and the left area and the right boundary are the O-phase and the T-phase, respectively. Because of the lattice mismatch between the two phases, as we obtained from Table S1,† in which the O-phase has a larger in-plane lattice parameter (a) but a smaller out-of-plane lattice parameter (c) than the T-phase, the lattice distortion can thus be observed. As seen in the enlarged view of area-1, the O-phase side has 13 lattice fringes, while the T-phase side has 12. Similarly, the O-phase side in area-2 has 9 lattice fringes, while the T-phase side has 10. Such an observation verified the results in Table S1.† Then we zoomed in area-3, circled in a red rectangle in Fig. S5,† and displayed it in Fig. 2(d). Because of the lattice mismatch, some B-site atoms in the lattice near the phase boundary have a larger displacement, as circled in the blue rectangles. The yellow and green dashed lines represent the real position of A-site and B-site atoms, respectively, and the blue dashed lines represent the middle position between two yellow lines. Obviously, the B-site atoms in these two areas have large upward displacements, which will lead to high polarization in the 0.7KNN–0.3BCZT ceramic. At this moment, we can almost ensure that the abnormal enhancement of polarization results from these high polarization boundaries (HPBs). Combined with the following equation,

$$P_i = P - P' = (\varepsilon_r - \varepsilon_{r\infty} - \varepsilon_{ro} - 1)\varepsilon_0 E = N(\alpha - \alpha_\infty - \alpha_o)E \quad (11)$$

which we deduced in the ESI,† the interfacial polarization is proportional to the applied field, and that is why the abnormal enhancement of polarization is more obvious in the 0.7KNN–0.3BCZT ceramic under 180 kV cm^{-1}.

3.4 Discussion of the electric breakdown strength with dielectric behaviors

The spheres in Fig. 5(a) show the variation between the E_b obtained from the result of the Weibull distribution ($E_{b\text{-}exp}$) and

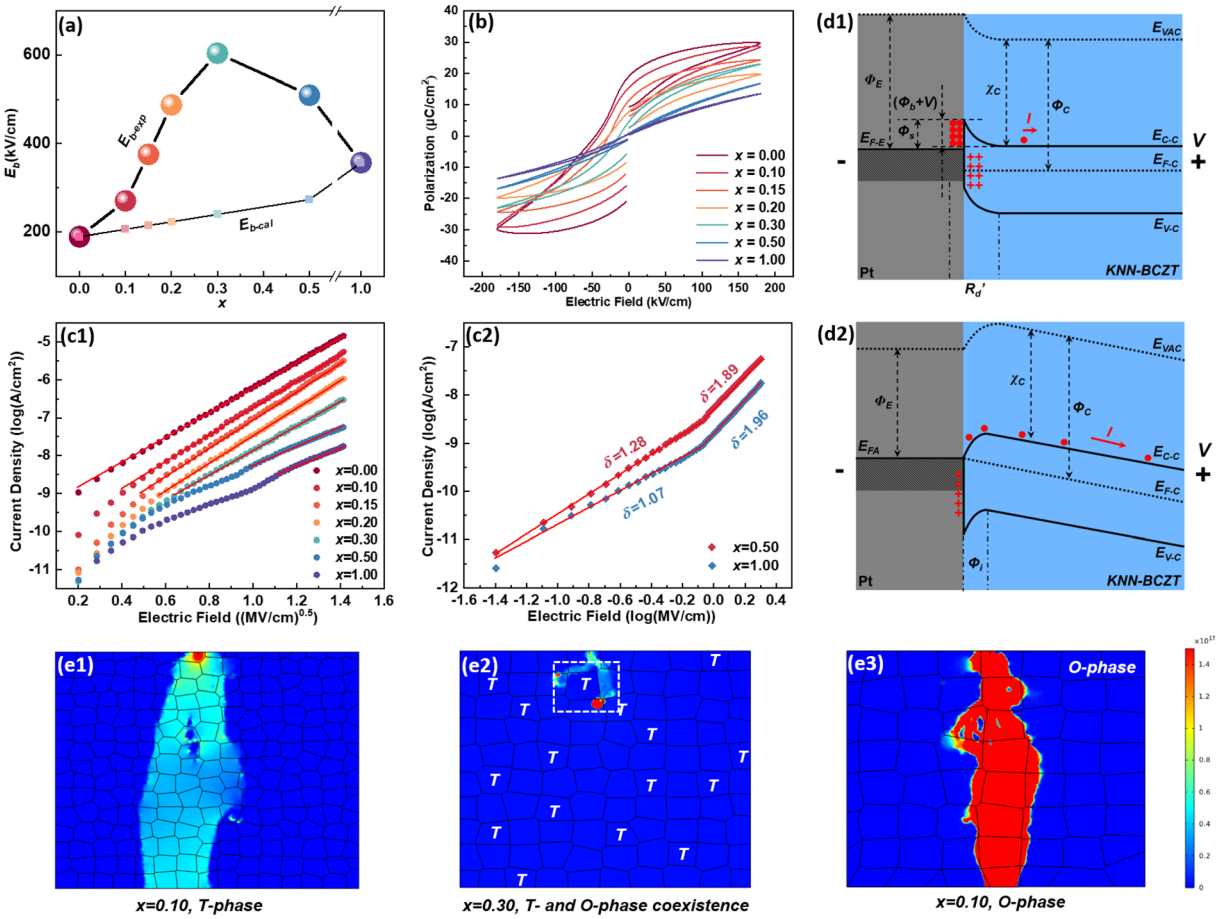

Fig. 5 (a) The variation between both $E_{b\text{-}exp}$ and $E_{b\text{-}cal}$ and x; (b) bipolar P–E loops of $(1-x)$KNN–xBCZT ceramics under 200 kV cm^{-1}; (c1) the fitting result of the J–E curves in Fig. S6† obtained according to (c1) eqn (13); (c2) eqn (14); band diagram to express the (d1) Schottky emission mode and (d2) ohmic contact mode under external bias. (e1)–(e3) The current density distribution of the $(1-x)$KNN–xBCZT ceramics with x = 0.10, 0.30, and 0.50 under 550 kV cm^{-1}, respectively.

the x, and in contrast, the variation between the calculated electric breakdown strength ($E_{b\text{-}cal}$) and the x is also plotted using smaller squares. The $E_{b\text{-}cal}$ was obtained according to the following equation:

$$E_{b\text{-}cal} = \frac{E_{b\text{-}BCZT} \times x_{BCZT} + E_{b\text{-}KNN} \times x_{b\text{-}KNN}}{x_{BCZT} + x_{KNN}} \quad (12)$$

in which $E_{b\text{-}BCZT}$ and $E_{b\text{-}KNN}$ are the experimental E_b of pristine BCZT and KNN ceramics, respectively, and $x_{max\text{-}BCZT}$ and $x_{max\text{-}KNN}$ are the molar ratios of BCZT and BZT parts in each $(1-x)$KNN–xBCZT ceramic, respectively. The physical significance of this equation is very simple: it shows how much extra voltage endurance can be obtained by BCZT dissolving into the KNN lattice when compared to the simple linear superposition of the two ceramic components. This figure shows that for simple linear superposition, the electric breakdown strength of $(1-x)$KNN–xBCZT ceramics should increase with increasing x. From the experimental result, however, it first increases with increasing x from 0.00 to 0.30 and then decreases with further x increment. Thus, we obviously cannot treat the electric breakdown strength of $(1-x)$KNN–xBCZT ceramics as a simple superposition. To reveal the physical mechanism inside, the bipolar P–E loops of all the ceramics were recorded, as shown in Fig. 5(b). Such bipolar loops of $(1-x)$KNN–xBCZT ceramics with smaller x have an opening between the starting and ending points, which signifies different ferroelectric behaviors under different voltage directions, and such an opening decreases with increasing x. Considering this, we measured the relationship between the current density and the electric field (J–E curves) of all the ceramics, as plotted in Fig. S6(a).† Then, we fit these J–E curves according to

$$J = A^*T^2 \exp\left[\frac{-q\left(\Phi_S - \sqrt{qE/4\pi\varepsilon_r\varepsilon_0}\right)}{kT}\right] \quad (13)$$

and

$$I = \sigma E \quad (14)$$

respectively, which are commonly used to determine the Schottky emission mode and the ohmic contact/space charge limited current (SCLC) mode in dielectric films. The J, Φ_S, E, T, and σ are the current density, Schottky barrier potential, electric

field across the material, absolute temperature, and electrical conductivity, respectively. The A^*, k, q, ε_0, and ε_r, which won't change with external factors, are the effective Richardson constant, Boltzmann constant, electronic charge, vacuum dielectric constant, and relative dielectric constant, respectively. In typical Schottky emission mode, the relationship between J and E in eqn (12) should be linear, while for eqn (13), the fitting result of σ equaling 1 and 2 indicates the conduction mechanism of ohmic contact mode and SCLC mode, respectively.[63] Fig. 5(c1) shows the fitting result of all the $(1-x)$KNN–xBCZT ceramics according to eqn (12) obtained by employing Origin 9 software. Although all the curves have a linear part, they deviate with increasing x, especially for 0.5KNN–0.5BCZT and pristine BCZT. Then, we fit the J–E curves of these two components according to eqn (13), and the segmented linear relationship with two different slopes was detected in both. The σ of 0.5KNN–0.5BCZT equals 1.28 and 1.89 under low and high electric fields, respectively, and that of pristine BCZT equals 1.07 and 1.96, respectively, as seen in Fig. 5(c2). The slope change signifies the transition of the conducting mechanism of these two components with increasing applied electric field. Before more discussion on it, which will be provided in the following part, at this moment, we can already provide quite a reasonable explanation of the variation in Fig. 5(a). For $(1-x)$KNN–xBCZT ceramics with smaller x, more electrons, which serve as the majority carriers, exist in the matrix and make them show n-type behavior. Additionally, based on the author's previous work and some other literature, the work function of the Pt electrode (Φ_E) is 5.56 eV, and the work function of KNN and BCZT is ~4.06 eV and ~4.8 eV (close to that of $BaTiO_3$), respectively,[64–66] resulting in the work function of $(1-x)$KNN–xBCZT ceramics (Φ_C) being between them. In this case, the ideal band diagram near the Pt/$(1-x)$KNN–xBCZT interface under applied bias can be depicted in Fig. 5(d1). A depletion region (R_d), which contains many trapped electrons, is formed at the interface. When the x is smaller, more electrons exist in the R_d, so its width is broader. Thus, the electrons have higher average mobility, and the ceramics break down more easily. When the x increases, as concluded from eqn (1)–(9), the number of electrons decreases, which makes the R_d thinner and the mobility lower, leading to higher E_b and the increment tendency before $x = 0.3$ in Fig. 5(a). For $(1-x)$KNN–xBCZT ceramics with a larger x of over 0.3, as mentioned above, a deviation happens. This is because the newly formed $V_O^{\cdot\cdot}$, as expressed in eqn (1)–(9), increases the electron affinity of the ceramics (χ_C) and their Fermi level ($E_{F\text{-}C}$) moves down. When the $E_{F\text{-}C}$ is lower than the Fermi level of the Pt electrode ($E_{F\text{-}E}$), the conduction mechanism will change from Schottky emission mode to ohmic contact mode, and the corresponding band diagram can be depicted in Fig. 5(d2).[67,68] All the applied voltage drops across the ceramic, and there is no depletion region in the Pt/$(1-x)$KNN–xBCZT interface anymore, with the loss of the trap effect to the electrons at the same time. Because of this, though the number of free electrons in $(1-x)$KNN–xBCZT ceramics decreases monotonously with increasing x, all the electrons in 0.5KNN–0.5BCZT and pristine BCZT are free to move in the whole ceramics, making the electric breakdown easier to happen when under higher electric fields, and finally leading to the decrement tendency after $x = 0.3$ as shown in Fig. 5(a). As abovementioned, the change of the slope in Fig. 5(c2) means the transition of the conducting mechanism for both 0.5KNN–0.5BCZT and pristine BCZT, and the conducting mechanism transfers from ohmic contact mode to SCLC mode with the electric field increasing. The details of the formation of these two band diagrams are shown in Fig. S7,† and the physical meaning of the abbreviations is also explained in the ESI.† In addition to the above reasons, compared to the other components, $(1-x)$KNN–xBCZT ceramics with $x = 0.3$ show two-phase coexistence, meaning that the interface area between the T-phase and O-phase also helps to increase its voltage endurance, which has already been proven by lots of studies.[69–71] Due to these two factors, 0.7KNN–0.3BCZT possesses the highest E_b of 604.07 kV cm^{-1}. To confirm such discussions above, the UV-vis absorption spectra of $(1-x)$KNN–xBCZT ceramics with $x = 0.1$, 0.3, and 0.5 are adopted, and the result is plotted in Fig. S6(b).† By employing the following formula:

$$(a\hbar v)^2 = A(\hbar v - E_g) \quad (15)$$

where $\hbar$, v, α, and A are the Planck constant, photon frequency, absorption factor, and a constant, respectively,[72] the band gap (E_g) of $(1-x)$KNN–xBCZT with $x = 0.1$, 0.3, and 0.5 was fitted to be 3.026 eV, 3.005 eV, and 2.970 eV, respectively, as seen in Fig. 6(a). For dielectrics, the E_g is normally positively proportional to their voltage endurance; this result agrees well with the tendency in Fig. 5(a), proving the correctness of our discussions above.[73] Besides, the reason for the best transparency in ceramics with $x = 0.3$, which we have mentioned above, can be revealed at this moment. On one hand, the transparency of polycrystalline ceramics increases with decreasing grain size for the decrement of pores, so the increasing BCZT dopant should improve the transparency of $(1-x)$KNN–xBCZT ceramics; on the other hand, one of the most fundamental conditions for transparency in ceramics is that the band-gap energy should be higher than 3.26 eV because in this case, the photon does not have sufficient energy to excite the valence electrons.[74–76]

To visually observe the difference in the electric breakdown behavior of the $(1-x)$KNN–xBCZT ceramics with different x under the effect of the conductive mechanism transition and interface engineering, computer simulation was applied using the finite element method through COMSOL Multiphysics 6.0 linked with Matlab 5.2. Fig. 5(e1)–(e3) depict the current density distribution of the $(1-x)$KNN–xBCZT ceramics with $x = 0.10$, 0.30, and 0.50 under 550 kV cm^{-1}, respectively. Based on the result of the Rietveld XRD refinement and the fitting result of the J–E curves, 0.9KNN–0.1BCZT and 0.5KNN–0.5BCZT were set to be a single T-phase and single O-phase, respectively, while 0.7KNN–0.3BCZT was set to be the coexistence of the T-phase and O-phase and the T-phase content was set to be ~38.32%. Besides, the conduction mode of 0.9KNN–0.1BCZT and 0.7KNN–0.3BCZT was set to be the Schottky emission, while that of 0.5KNN–0.5BCZT was set as ohmic contact. More details on the physical model of such a simulation are explained in the ESI.† From the result, we can see that expect 0.7KNN–0.3BCZT,

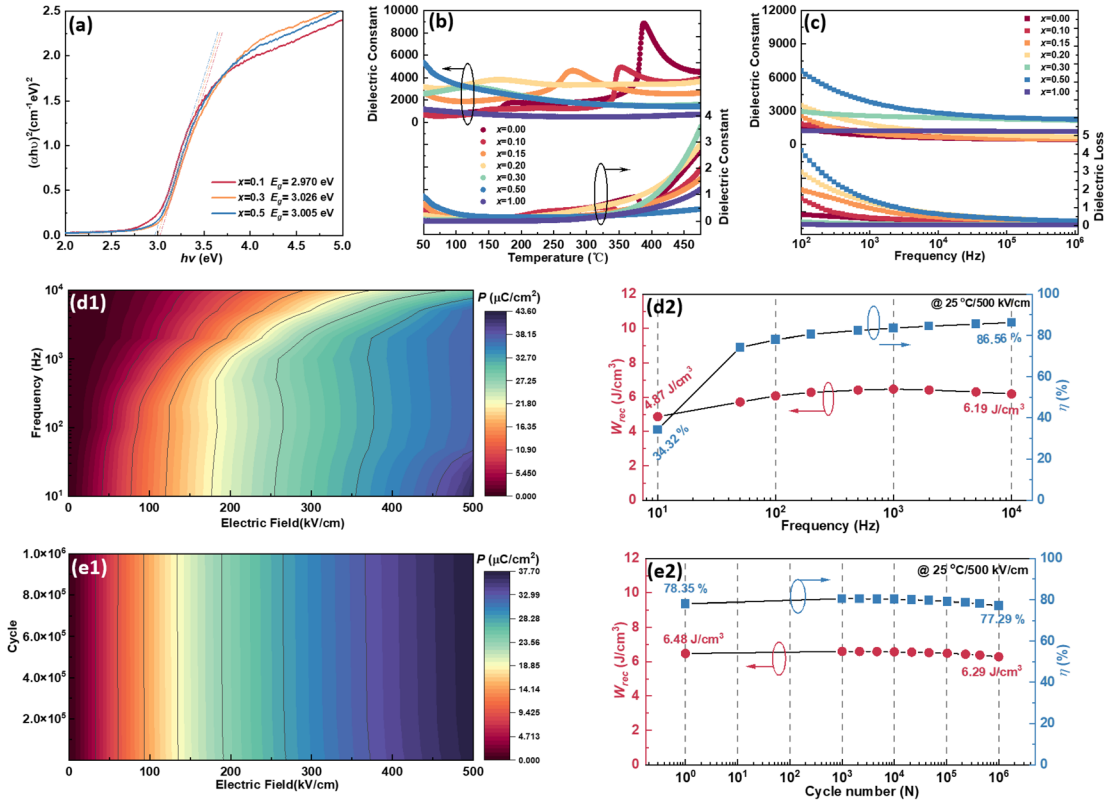

Fig. 6 (a) The fitting results of Fig. S6† according to eqn (15) to obtain the E_g of $(1-x)$KNN–xBCZT with $x = 0.1$, 0.3, and 0.5; (b) the ε–T curves with tan δ–T curves of the $(1-x)$KNN–xBCZT ceramics from 50 °C to 475 °C at 1000 Hz; (c) the ε–f curves with the tan δ–f curves of the $(1-x)$KNN–xBCZT ceramics from 10^2 to 10^6 Hz at room temperature; (d1) the mapping to show the variation between polarization and both the applied frequency and the electric field; (d2) the variation between both W_{rec} and η and frequency; (e1) the mapping to show the variation between polarization and both the cycling number and the electric field; (e2) the variation between both W_{rec} and η and the cycling number.

both the other two components were broken down, and interfaces between the T-phase and O-phase in 0.7KNN–0.3BCZT indeed have blocking behavior to the spread of the current, as marked by the white dashed rectangle. The result of the finite element simulation agrees well with the experimental result. Fig. S8(a1)–(a3) and (b1)–(b3)† display the distribution of the electric potential and electric field of these three ceramics under 550 kV cm^{-1}, respectively. The excellent electric breakdown strength of the 0.7KNN–0.3BCZT ceramic is caused by the combined effect of the conductive mechanism transition and interface engineering.

3.5 Characterization of the energy storage reliability with charge–discharge behavior

Fig. S9† displays the temperature dependence of the dielectric constant (ε–T curve) and dielectric loss (tan δ–T curve) of all the $(1-x)$KNN–xBCZT ceramics from 50 °C to 475 °C at different frequencies, and the curve at 1000 Hz of each component is picked up and summarized in Fig. 6(b). With x increasing, the Curie temperature (T_c) of $(1-x)$KNN–xBCZT ceramics shifts to lower temperatures, and the transition peaks start to overlap. Meanwhile, the frequency dispersion, phase transition diffusion, and ε decrement are also observed, manifesting the typical ferroelectric to relaxor ferroelectric (FE-to-RFE) phase transition. Fig. 6(c) plots the frequency dependence of ε (ε–f curve) and tan δ(tan δ–f curve) of all the $(1-x)$KNN–xBCZT ceramics from 10^2 Hz to 10^6 Hz. As a typical FE or RFE, the ε decreases with increasing f, and compared to the other components, 0.7KNN–0.3BCZT shows the best dielectric frequency stability.

Good dielectric frequency stability would also benefit the energy storage stability. To prove and characterize this, we recorded the unipolar P–E loops of 0.7KNN–0.3BCZT measured from 10^2 Hz to 10^4 Hz under 500 kV cm^{-1} at room temperature. All these loops are shown in Fig. S10(a),† and the variation between polarization and both the applied frequency and the electric field during the voltage ramping up is summarized in a mapping, as displayed in Fig. 6(d1). The polarization increases from the top left to the bottom right. After integration, the variation between the energy storage performance (W_{rec} and η) and applied frequency is plotted in Fig. 6(d2), and the decrement of W_{rec} in this whole frequency range is only 21.32%. Energy storage performance after long-term use is also an essential factor in characterizing the reliability of a capacitor, and the unipolar P–E loops of 0.7KNN–0.3BCZT obtained during polarization fatigue from the 1st to the 10^{6th} cycle under 500 kV cm^{-1} are shown in Fig. S10(b).† The mapping of the variation between polarization and both the cycling number and the electric field during the voltage ramping up is displayed in Fig. 6(e1), and the vertical stripes can be clearly seen, which manifest excellent polarization fatigue endurance. Fig. 6(e2)

plots the cycling number dependent on the energy storage performance, and the decrement of W_{rec} is only 2.93%.

To characterize the energy storage thermal stability, the unipolar *P–E* loops of the 0.7KNN–0.3BCZT ceramic measured from room temperature to 200 °C at 500 kV cm^{-1} were recorded and are shown in Fig. S11(a),† and the mapping of polarization variation with the electric field and temperature during the voltage ramping up is displayed in Fig. 7(a1). As seen, the polarization measured under the same electric field increases slightly with increasing temperature, and such behavior becomes more obvious at higher electric fields, which is thought to be attributed to the thermally activated dipole polarization.[77,78] Fig. 7(a2) plots the temperature dependence of the energy storage performance. Both W_{rec} and η decrease very slowly with increasing temperature, and the decrement is only 9.69% and 11.58%, respectively. Further characterization of reliability is focused on the polarization fatigue endurance in high-temperature environments, so the unipolar *P–E* loops of the 0.7KNN–0.3BCZT ceramic obtained during polarization fatigue from the 1st to the 10^{6th} cycle under 500 kV cm^{-1} at 200 ° C were measured and are shown in Fig. S11(b).† Similar to the fatigue characterization at room temperature, the vertical stripes on the mappings also indicate the polarization fatigue stability at 200 °C under long-term use, as displayed in Fig. 7(b1). After integration, as shown in Fig. 7(b2), the W_{rec} and η decrement is only 2.93% and 6.48%, respectively.

The practical application performance of BCZT–0.15BZT as an energy storage capacitor was determined through an *R–L–C* circuit with a load resistance (R_L) of 100 Ω using the pulsed charge–discharge test. The underdamped and overdamped current discharge curves obtained under various electric fields of the 0.7KNN–0.3BCZT ceramic are shown in Fig. 7(c) and (d), respectively, and an apparent complete oscillation can be seen in the former while only a positive peak exists in the latter. For the underdamped circumstance, according to the formulae below:

$$C_D = \frac{I_{max}}{S} \quad (16)$$

$$P_D = \frac{EI_{max}}{2S} \quad (17)$$

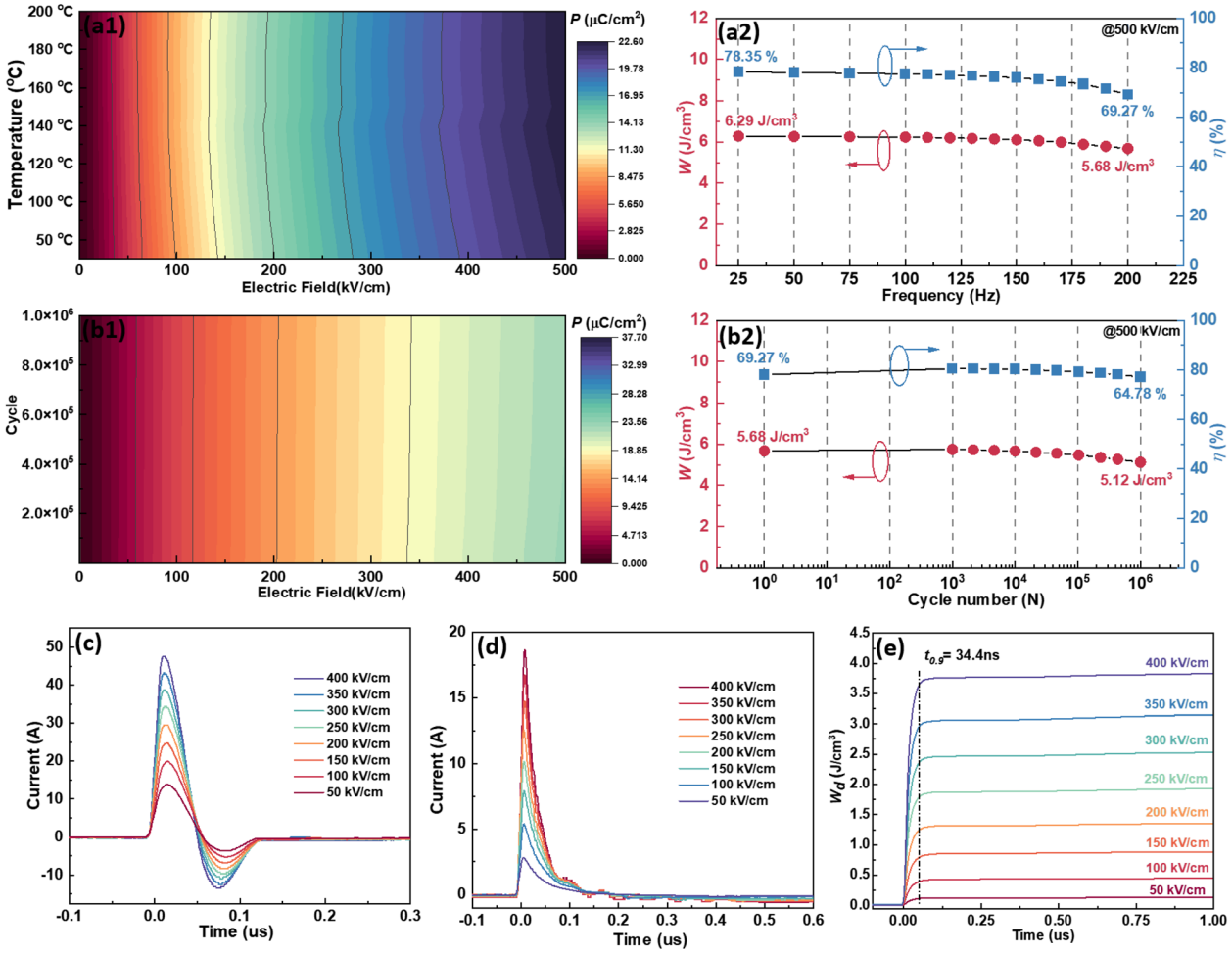

Fig. 7 (a1) The mapping to show the variation between polarization and both temperature and the electric field; (a2) the variation between both W_{rec} and η and temperature; (b1) the mapping to show the variation between polarization and both the cycling number and the electric field at 200 °C; (b2) the variation between both W_{rec} and η and the cycling number at 200 °C; the (c) underdamped and (d) overdamped current discharge curves obtained under various electric fields of the 0.7KNN–0.3BCZT ceramic; (e) the time dependence of the W_D of the 0.7KNN–0.3BCZT ceramic under different electric fields.

the electric field dependence of current (I_{max}), current density (C_D), and power density (P_D) was obtained and is plotted in Fig. S12.† Their maximum value reaches 47.6 A, 752.6 A cm^{-2}, and 77.7 MW cm^{-3} at 400 kV cm^{-1}, respectively, as plotted in Fig. S12.† For the overdamped circumstance, using the formula below,

$$W_D = R\int i^2 t \mathrm{d}t/V \quad (18)$$

in which R, V, I, and t are the load resistance, sample volume, discharge current, and time, respectively, the time dependence of the discharge energy density (W_D) of the 0.7KNN–0.3BCZT ceramic under different electric fields was calculated and is plotted in Fig. 7(e), and the W_D values are all lower than the corresponding W_{rec} when compared with Fig. 3(b). The W_D (3.75 J cm^{-3}) calculated here is lower than the value calculated using the static method, which is around ∼6.00 J cm^{-3}, as seen in Fig. 3(b). This is due to the clamping effect on the ferroelectric domains, which has been reported frequently elsewhere.[79] The $t_{0.9}$, which is the time required for dielectric capacitors to release 90% of the total energy stored, was observed to be ∼34.4 ns, indicating that the 0.7KNN–0.3BCZT ceramic is a promising candidate for pulsed power capacitor applications.

4 Conclusions and prospects

$(1-x)$KNN–xBCZT transparent ceramics were synthesized through conventional solid-state technology, and the intrinsic high leakage current of pristine KNN ceramic was decreased by the inhibition of the formation of electrons after doping BCZT, which was proved by defect equations. A W_{rec} of 7.83 J cm^{-3} with an η of 81.02% was finally achieved in the $(1-x)$KNN–xBCZT ceramics with $x = 0.30$ through multiscale designing, and after the characterization of the structure and properties, analysis of the band diagram, and finite element simulation on COMSOL Multiphysics 6.0, the reason for such a good energy storage performance was revealed to be both large P_{max} and high E_b. Specifically, the former was caused by HPBs, which were induced by the lattice mismatch between the T-phase and O-phase and were directly observed from the TEM images; the latter was caused by the combined effect of conductive mechanism transition and interface engineering, which was proved by employing the band diagram and computer simulation. After comparing, our ceramics show quite a huge potential when serving as energy storage capacitors among both BCZT- and KNN-based systems. For reliability characterization, the 0.7KNN–0.3BCZT ceramic shows quite good frequency stability, thermal stability, and polarization fatigue endurance at both room temperature and 200 °C. Besides, good charge–discharge behavior with a $t_{0.9}$ of ∼34.4 ns was also obtained in the 0.7KNN–0.3BCZT ceramic, demonstrating its potential in practical applications.

Author contributions

Zixiong Sun: conceptualization, methodology, writing-reviewing and editing, supervision, and funding acquisition. Shibo Zhao: data curation. Hongmei Jing: writing-reviewing and editing. Qing Guo: software. Ruyue Gao: data curation. Liming Diwu: data curation. Kang Du: Rietveld XRD refinement. Yongping Pu: funding acquisition and supervision.

Conflicts of interest

The authors declared that they have no conflicts of interest in this work.

Acknowledgements

This work was financed by the National Natural Science Foundation of China (52002234), Open Foundation of Hubei Key Laboratory of Micro-Nanoelectronic Materials and Devices (K202313), Open Foundation of Key Laboratory of Auxiliary Chemistry and Technology for Chemical Industry, Ministry of Education, Shaanxi University of Science and Technology (No. KFKT2021-09), and Shaanxi Collaborative Innovation Center of Industrial Auxiliary Chemistry and Technology.

References

1 T. Zhang, H. Sun, C. Yin, Y. H. Jung, S. Min, Y. Zhang, C. Zhang, Q. Chen, K. J. Lee and Q. Chi, *Prog. Mater. Sci.*, 2023, **140**, 101207.
2 J. Chen, Z. Pei, B. Chai, P. Jiang, L. Ma, L. Zhu and X. Huang, *Adv. Mater.*, 2023, 2308670.
3 X. Wang, F. Yang, K. Yu, B. Zhang, J. Chen, Y. Shi, P. Yang, L. He, H. Li, R. Liu, X. Li, Y. Hu, J. Shang and S. Yin, *Adv. Mater. Technol.*, 2023, **8**, 2202044.
4 Z. Sun, H. Wei, S. Zhao, Q. Guo, Y. Bai, S. Wang, P. Sun, K. Du, Y. Ning, Y. Tian, X. Zhang, H. Jing, Y. Pu and S. Zhang, *J. Mater. Chem. A*, 2024, **12**, 128–143.
5 Y. Gao, W. Qiao, X. Lou, Z. Song, X. Zhu, L. He, B. Yang, Y. Hu, J. Shao, D. Wang, Z. Chen and S. Zhang, *Adv. Mater.*, 2023, **36**, 2310559.
6 Z. Sun, Z. Wang, Y. Tian, G. Wang, W. Wang, M. Yang, X. Wang, F. Zhang and Y. Pu, *Adv. Electron. Mater.*, 2019, **6**, 1900698.
7 Y. Ning, Y. Pu, C. Wu, Z. Chen, X. Zhang, L. Zhang and B. Wang, *J. Eur. Ceram. Soc.*, 2024, **44**, 4831–4833.
8 Z. Sun, S. Wang, S. Zhao, H. Wei, G. Shen, Y. Pu and S. Zhang, *J. Mater. Chem. C*, 2024, **12**, 859–867.
9 W. Wang, L. Zhang, Y. Yang, W. Shi, Y. Huang, D. O. Alikin, V. Ya. Shur, Z. Lou, A. Zhang, X. Wei, D. Wang, F. Gao, H. Du and L. Jin, *J. Mater. Chem. A*, 2023, **11**, 2641–2651.
10 F. Yan, G. Ge, J. Qian, J. Lin, C. Chen, Z. Liu and J. Zhai, *Small*, 2022, **19**, 2206125.
11 Z. Sun, Y. Bai, J. Liu, G. Jian, C. Guo, L. Zhang and Y. Pu, *J. Alloys Compd.*, 2022, **909**, 164735.
12 Z. Sun, C. Ma, M. Liu, J. Cui, L. Lu, J. Lu, X. Lou, L. Jin, H. Wang and C. Jia, *Adv. Mater.*, 2016, **29**, 27897340.
13 M. D. Nguyen, Y. A. Birkhölzer, E. P. Houwman, G. Koster and G. Rijnders, *Adv. Energy Mater.*, 2022, **12**, 2200517.

14 Z. Sun, Y. Bai, H. Jing, T. Hu, K. Du, Q. Guo, T. Ye, C. Ma, M. Liu and Y. Pu, *Mater. Horiz.*, 2024, DOI: 10.1039/d4mh00322e.
15 X. Nie, Y. He, Q. Shi, Y. Liang, L. Wei, P. Liang, X. Chao, G. Hu and Z. Yang, *J. Adv. Dielectr.*, 2023, **13**, 2242005.
16 Q. Chai, F. Zhang, Q. Zhou, Z. Peng, D. Wu, P. Liang, L. Wei, X. Chao and Z. Yang, *Small*, 2023, **19**, 2207464.
17 X. Ren, L. Jin, Z. Peng, B. Chen, X. Qiao, D. Wu, G. Li, H. Du, Z. Yang and X. Chao, *Chem. Eng. J.*, 2020, **390**, 124566.
18 M. Zhang, H. Yang, D. Li and Y. Lin, *J. Alloys Compd.*, 2020, **829**, 154565.
19 J. Lin, G. Ge, K. Zhu, H. Bai, B. Sa, F. Yan, G. Li, C. Shi, J. Zhai, X. Wu and Q. Zhang, *Chem. Eng. J.*, 2022, **444**, 136538.
20 Z. Cen, X. Wang, Y. Huan and L. Li, *J. Am. Ceram. Soc.*, 2018, **101**, 2391–2407.
21 Z. Sun, Y. Bai, T. Ouyang, Q. Guo, Y. Ning, J. Liu, H. Wei, K. Du, H. Jing, Y. Tian and Y. Pu, *Appl. Phys. Lett.*, 2023, **122**, 263904.
22 Y. Peng, Z. Tan, J. An, J. Zhu and Q. Zhang, *J. Eur. Ceram. Soc.*, 2019, **39**, 5252–5259.
23 D. Zhang, D. Sando, P. Sharma, X. Cheng, F. Ji, V. Govinden, M. Weyland, V. Nagarajan and J. Seidel, *Nat. Commun.*, 2020, **11**, 349.
24 Y. Ning, Y. Pu, C. Wu, S. Zhou, L. Zhang, J. Zhang, X. Zhang and Y. Shang, *J. Mater. Sci. Technol.*, 2023, **145**, 66.
25 W. Wang, L. Zhang, R. Jing, Q. Hu, D. O. Alikin, V. Ya. Shur, X. Wei, G. Liu, Y. Yan and L. Jin, *Chem. Eng. J.*, 2022, **434**, 134678.
26 H. Pan, S. Lan, S. Xu, Q. Zhang, H. Yao, Y. Liu, F. Meng, E.-J. Guo, L. Gu and D. Yi, *Science*, 2021, **374**, 100.
27 A. K. Yadav, C. T. Nelson, S. L. Hsu, Z. Hong, J. D. Clarkson, C. M. Schlepütz, A. R. Damodaran, P. Shafer, E. Arenholz and L. R. Dedon, *Nature*, 2016, **530**, 198.
28 T. Wang, L. Jin, C. Li, Q. Hu and X. Wei, *J. Am. Ceram. Soc.*, 2014, **98**, 559.
29 K. Xu, P. Yang, W. Peng, L. Li and J. Alloy, *Compd*, 2020, **829**, 116.
30 D. Han, C. Wang, Z. Zeng, X. Wei, P. Wang, Q. Liu, D. Wang, F. Meng and J. Alloy, *Compd*, 2020, **902**, 163721.
31 Z. Chen, Y. Pu, Y. Ning, C. Wu, L. Zhang, X. Zhang and B. Wang, *Ceram. Int.*, 2023, **49**, 34520.
32 M. Zhou, R. Liang, Z. Zhou and X. Dong, *J. Mater. Chem. C*, 2018, **6**, 8528.
33 A. R. Jayakrishnan, P. V. K. Yadav, J. P. B. Silva and K. C. Sekhar, *J. Sci.: Adv. Mater. Devices*, 2020, **5**, 119.
34 X. Fan, P. Li, J. Du, C. Chen, P. Fu, J. Hao, Z. Xue and W. Li, *J. Mater. Sci.: Mater. Electron.*, 2020, **31**, 9974.
35 A. Jain, Y. G. Wang and H. Guo, *Ceram. Int.*, 2020, **46**, 24333.
36 Q. Yuan, G. Li, F. Yao, S. Cheng, Y. Wang, R. Ma, S. Mi, M. Gu, J. Li and H. Wang, *Nano Energy*, 2018, **52**, 203–210.
37 V. S. Puli, D. K. Pradhan, B. C. Riggs, D. B. Chrisey and R. S. Katiyar, *Integr. Ferroelectr.*, 2014, **157**, 139.
38 H. Yang, F. Yan, G. Zhang, Y. Lin, F. Wang and J. Alloy, *Compd*, 2017, **720**, 116.
39 A. Jain, Y. Wang, N. Wang and F. Wang, *Ceram. Int.*, 2020, **46**, 28800.
40 S. N. Norkar, P. Aggarwal and V. K. Deshpande, *Curr. Appl. Phys.*, 2022, **39**, 250.
41 C. Shi, F. Yan, G. Ge, Y. Wei, J. Zhai and W. Yao, *Chem. Eng. J.*, 2021, **426**, 130800.
42 Z. Dai, J. Xie, Z. Chen, S. Zhou, J. Liu, W. Liu, Z. Xi and X. Ren, *Chem. Eng. J.*, 2021, **410**, 128341.
43 J. Song, F. Yan, J. Lin, G. Ge, C. Shi, J. Qian, Y. Hao, Y. Wei and W. Yao, *Chem. Eng. J.*, 2023, **474**, 145754.
44 Y. Huan, T. Wei, X. Wang, X. Liu, P. Zhao and X. Wang, *Chem. Eng. J.*, 2021, **425**, 129506.
45 R. Hu, Y. Lin, M. Zhang, Q. Yuan and H. Yang, *Mater. Today Energy*, 2022, **30**, 101185.
46 Q. Chen, T. Gao, R. Lang, Z. Tan, J. Xing and J. Zhu, *J. Eur. Ceram. Soc.*, 2023, **43**, 2442–2451.
47 M. Zhang, H. Yang, D. Li, L. Ma and Y. Lin, *J. Mater. Chem. C*, 2020, **8**, 8777–8785.
48 B. Qu, H. Du and Z. Yang, *J. Mater. Chem. C*, 2016, **4**, 1795–1803.
49 L. Dong, Z. Dai, J. Hou, C. Liu, R. Dai, Y. Liu, W. Liu and S. Gu, *J. Energy Storage*, 2023, **74**, 109527.
50 C. Li, Y. Huan, X. Wang, X. Wang, T. Wang and T. Wei, *J. Am. Ceram. Soc.*, 2022, **105**, 6158–6167.
51 B. Qu, H. Du and Z. Yang, *J. Mater. Chem. C*, 2016, **4**, 1795–1803.
52 L. Wu, Y. Huan, C. Li, F. Jiang and T. Wei, *Ceram. Int.*, 2023, **49**, 22015–22021.
53 L. Wu, Y. Huan, X. Wang, C. Li, Y. Luo and T. Wei, *J. Mater. Sci.*, 2022, **57**, 15876–15888.
54 Z. Yang, F. Gao, H. Du, L. Jin, L. Yan, Q. Hu, Y. Yu, S. Qu, X. Wei, Z. Xu and Y.-J. Wang, *Nano Energy*, 2019, **58**, 768–777.
55 B. Qu, H. Du and Z. Yang, *J. Mater. Chem. C*, 2016, **4**, 1795–1803.
56 B. Qu, H. Du, Z. Yang and Q. Liu, *J. Am. Ceram. Soc.*, 2017, **100**, 1517–1526.
57 Z. Cen, S. Bian, Z. Xu, K. Wang, L. Guo, L. Li and X. Wang, *J. Adv. Ceram.*, 2021, **10**, 820–831.
58 A. P. Espinosa, L. Ramajo, F. Rubio-Marcos, C. Macchi, A. Somoza and M. Castro, *J. Eur. Ceram. Soc.*, 2021, **41**, 1288–1298.
59 Y. Guo, K. Kakimoto and H. Ohsato, *Jpn. J. Appl. Phys.*, 2004, **43**, 6662.
60 G. Wang, J. Zheng, H. Bi, S. Wang, J. Wang, J. Sun, Y. Guo and C. Wang, *Scr. Mater.*, 2019, **162**, 28–32.
61 L.-B. Xiong, J.-L. Li, B. Yang and Y. Yu, *J. Nanomater.*, 2012, **2012**, 9.
62 S. Wang, L. Pan, J.-J. Song, W. Mi, J.-J. Zou, L. Wang and X. Zhang, *J. Am. Chem. Soc.*, 2015, **137**, 2975–2983.
63 F.-C. Chiu, *Adv. Mater. Sci. Eng.*, 2014, **2014**, 578168.
64 F. Opoku, K. K. Govender, C. G. van Sittert and P. P. Govender, *Carbon*, 2018, **136**, 187–195.
65 Z. Sun, S. Huang, W. Zhu, Y. A. Birkhölzer, X. Gao, R. A. Avila, H. Huang, X. Lou, E. P. Houwman, M. D. Nguyen, G. Koster and G. Rijnders, *APL Mater.*, 2023, **11**, 101129.
66 Z. Sun, E. P. Houwman, S. Wang, M. D. Nguyen, G. Koster and G. Rijnders, *J. Alloys Compd.*, 2024, **981**, 173758.
67 X. Ding, Y. Zhao, H. Xiao and L. Qiao, *Appl. Phys. Lett.*, 2021, **118**, 091601.

68 G. Jiang, X. Hu and L. Sun, *ACS Appl. Electron. Mater.*, 2023, **5**, 3071–3077.
69 Z. Sun, J. Liu, H. Wei, Q. Guo, Y. Bai, S. Zhao, S. Wang, L. Li, Y. Zhang, Y. Tian, X. Zhang, H. Jing, Y. Pu and S. Zhang, *J. Mater. Chem. A*, 2024, **12**, 128–143.
70 P. Wang, X. Wang, G. Li, Y. Li, X. Yao and Z. Pan, *Chem. Eng. J.*, 2022, **433**, 133676.
71 Y. Ning, Y. Pu, C. Wu, Z. Chen, X. Zhang, L. Zhang and B. Wang, *J. Eur. Ceram. Soc.*, 2024, **44**, 4831–4843.
72 M. Wang, Y. Lin, Q. Yuan, M. Zhang, Y. Yu, F. Yan and H. Yang, *Inorg. Chem. Front.*, 2023, **10**, 4578–4586.
73 L. Wu, Y. Huan, X. Wang, C. Li, Y. Luo and T. Wei, *J. Mater. Sci.*, 2022, **57**, 15876–15888.
74 S. F. Wang, J. Zhang, D. W. Luo, F. Gu, D. Y. Tang, Z. L. Dong, G. E. B. Tan, W. X. Que, T. S. Zhang, S. Li and L. B. Kong, *Prog. Solid State Chem.*, 2013, **41**, 20–54.
75 A. M. Tsabit and D.-H. Yoon, *J. Korean Ceram. Soc.*, 2021, **59**, 1–24.
76 Z. Xiao, S. Yu, Y. Li, S. Ruan, L. B. Kong, Q. Huang, Z. Huang, K. Zhou, H. Su, Z. Yao, W. Que, Y. Liu, T. Zhang, J. Wang, P. Liu, D. Shen, M. Allix, J. Zhang and D. Tang, *Mater. Sci. Eng., R*, 2020, **139**, 100518.
77 B. Li, T. Zheng and J. Wu, *ACS Appl. Mater. Interfaces*, 2021, **13**, 37422–37432.
78 Y. Zhang, X. L. Zhong, M. Vopson, J. B. Wang and Y. C. Zhou, *J. Appl. Phys.*, 2012, **112**, 014112.
79 L. Yang, X. Kong, F. Li, H. Hao, Z. Cheng, H. Liu, J.-F. Li and S. Zhang, *Prog. Mater. Sci.*, 2019, **102**, 72.